

Dual-Color Fluorescence Cross-Correlation Spectroscopy on a Single Plane Illumination Microscope (SPIM-FCCS)

Jan Wolfgang Krieger,¹ Anand Pratap Singh,² Christoph S. Garbe,³
Thorsten Wohland² and Jörg Langowski,^{1,*}

¹German Cancer Research Center (DKFZ), Biophysics of Macromolecules (B040), Im
Neuenheimer Feld 580, D-69120 Heidelberg, Germany

²Departments of Biological Sciences and Chemistry and NUS Centre for BioImaging
Sciences, National University of Singapore, 14 science Drive 4, Singapore 117557

³Interdisciplinary Center for Scientific Computing, University of Heidelberg, Speyerer Straße
6, D-69115 Heidelberg, Germany

* jl@dkfz.de

<http://www.dkfz.de/Macromol>

Abstract: Single plane illumination microscopy based fluorescence correlation spectroscopy (SPIM-FCS) is a new method for imaging FCS in 3D samples, providing diffusion coefficients, flow velocities and concentrations in an imaging mode. Here we extend this technique to two-color fluorescence cross-correlation spectroscopy (SPIM-FCCS), which allows to measure molecular interactions in an imaging mode. We present a theoretical framework for SPIM-FCCS fitting models, which is subsequently used to evaluate several test measurements of *in-vitro* (labeled microspheres, several DNAs and small unilamellar vesicles) and *in-vivo* samples (dimeric and monomeric dual-color fluorescent proteins, as well as membrane bound proteins). Our method yields the same quantitative results as the well-established confocal FCCS, but in addition provides unmatched statistics and true imaging capabilities.

© 2014 Optical Society of America

OCIS codes: (040.1490) Cameras; (180.2520) Fluorescence microscopy; (180.6900) Three-dimensional microscopy; (300.6280) Spectroscopy, fluorescence and luminescence.

References and links

1. D. Magde, E. L. Elson, and W. W. Webb, "Fluorescence correlation spectroscopy I: Conceptual basis and theory," *Biopolymers* **13**, 1–27 (1974).
2. D. Magde, E. L. Elson, and W. W. Webb, "Fluorescence correlation spectroscopy. II. an experimental realization." *Biopolymers* **13**, 29–61 (1974).
3. K. M. Berland, P. T. So, and E. Gratton, "Two-photon fluorescence correlation spectroscopy: method and application to the intracellular environment," *Biophys. J.* **68**, 694–701 (1995).
4. P. Schwille, F. Meyer-Almes, and R. Rigler, "Dual-color fluorescence cross-correlation spectroscopy for multi-component diffusional analysis in solution," *Biophys. J.* **72**, 1878 – 1886 (1997).
5. U. Kettling, A. Koltermann, P. Schwille, and M. Eigen, "Real-time enzyme kinetics monitored by dual-color fluorescence cross-correlation spectroscopy," *Proc. Natl. Acad. Sci.* **95**, 1416–1420 (1998).
6. K. G. Heinze, M. Jahnz, and P. Schwille, "Triple-color coincidence analysis: One step further in following higher order molecular complex formation," *Biophys. J.* **86**, 506 – 516 (2004).

7. L. C. Hwang, M. Gösch, T. Lasser, and T. Wohland, "Simultaneous multicolor fluorescence cross-correlation spectroscopy to detect higher order molecular interactions using single wavelength laser excitation," *Biophys. J.* **91**, 715–727 (2006).
8. F. Bestvater, Z. Seghiri, M. S. Kang, N. Gröner, J. Y. Lee, I. Kang-Bin, and M. Wachsmuth, "EMCCD-based spectrally resolved fluorescence correlation spectroscopy," *Opt. Express* **18**, 23818–23828 (2010).
9. D. M. Shcherbakova, M. A. Hink, L. Joosen, T. W. J. Gadella, and V. V. Verkhusha, "An orange fluorescent protein with a large Stokes shift for single-excitation multicolor FCCS and FRET imaging," *J. Am. Chem. Soc.* **134**, 7913–7923 (2012).
10. O. Krichevsky and G. Bonnet, "Fluorescence correlation spectroscopy: the technique and its applications," *Rep. Prog. Phys.* **65**, 251–297 (2002).
11. K. Bacia, S. A. Kim, and P. Schwille, "Fluorescence cross-correlation spectroscopy in living cells," *Nat. Methods* **3**, 83–89 (2006).
12. E. Haustein and P. Schwille, "Fluorescence correlation spectroscopy: novel variations of an established technique," *Annu. Rev. Biophys. Biomol. Struct.* **36**, 151–169 (2007).
13. N. Dross, C. Spriet, M. Zwerger, G. Müller, W. Waldeck, and J. Langowski, "Mapping eGFP oligomer mobility in living cell nuclei," *PLoS ONE* **4**, e5041 (2009).
14. J. Ries, S. Chiantia, and P. Schwille, "Accurate determination of membrane dynamics with line-scan FCS," *Biophys. J.* **96**, 1999–2008 (2009).
15. Q. Ruan, M. A. Cheng, M. Levi, E. Gratton, and W. W. Mantulin, "Spatial-temporal studies of membrane dynamics: Scanning fluorescence correlation spectroscopy (SFCS)," *Biophys. J.* **87**, 1260–1267 (2004).
16. G. Heuvelman, F. Erdel, M. Wachsmuth, and K. Rippe, "Analysis of protein mobilities and interactions in living cells by multifocal fluorescence fluctuation microscopy," *Eur. Biophys. J.* **38**, 813–828 (2009).
17. D. J. Needleman, Y. Xu, and T. J. Mitchison, "Pin-hole array correlation imaging: Highly parallel fluorescence correlation spectroscopy," *Biophys. J.* **96**, 5050–5059 (2009).
18. R. A. Colyer, G. Scalia, I. Rech, A. Gulinatti, M. Ghioni, S. Cova, S. Weiss, and X. Michalet, "High-throughput FCS using an LCOS spatial light modulator and an 8×1 spad array," *Biomed. Opt. Express* **1**, 1408–1431 (2010).
19. M. Kloster-Landsberg, D. Tyndall, I. Wang, R. Walker, J. Richardson, R. Henderson, and A. Delon, "Note: Multifocal fluorescence correlation spectroscopy in living cells using a complementary metal oxide semiconductor-single photon avalanche diode array," *Rev. Sci. Instrum.* **84**, 076105 (2013).
20. B. Kannan, L. Guo, T. Sudhakaran, S. Ahmed, I. Maruyama, and T. Wohland, "Spatially resolved total internal reflection fluorescence correlation microscopy using an electron multiplying charge-coupled device camera," *Anal. Chem.* **79**, 4463–4470 (2007).
21. T. Wohland, X. Shi, J. Sankaran, and E. H. K. Stelzer, "Single plane illumination fluorescence correlation spectroscopy (SPIM-FCS) probes inhomogeneous three-dimensional environments," *Opt. Express* **10**, 10627–10641 (2010).
22. J. Capoulade, M. Wachsmuth, L. Hufnagel, and M. Knop, "Quantitative fluorescence imaging of protein diffusion and interaction in living cells," *Nat. Biotechnol.* **29**, 835–839 (2011).
23. SI: The supplementary notes are available at <http://www.dkfz.de/Macromol/publications/files/spimfcs2013-supplement.pdf>.
24. M. Gösch, A. Magnusson, S. Hård, H. Blom, S. Anderegg, K. Korn, P. Thyberg, M. Wells, T. Lasser, and R. Rigler, "Parallel dual-color fluorescence cross-correlation spectroscopy using diffractive optical elements," *J. Biomed. Opt.* **10**, 054008 (2005).
25. J. Ries, Z. Petrášek, A. J. García-Sáez, and P. Schwille, "A comprehensive framework for fluorescence cross-correlation spectroscopy," *New J. Phys.* **12**, 113009 (2010).
26. V. Betaneli, E. P. Petrov, and P. Schwille, "The role of lipids in VDAC oligomerization," *Biophys. J.* **102**, 523–531 (2012).
27. P. W. Wiseman, J. A. Squier, and K. R. Wilson, "Dynamic image correlation spectroscopy (ICS) and two-color image cross-correlation spectroscopy (ICCS): concepts and application," in "BiOS 2000 Int. Symp. Biomed. Opt.", (Int. Soc. Opt. Photon., 2000), pp. 14–20.
28. T. Toplak, E. Pandzic, L. Chen, M. Vicente-Manzanares, A. R. Horwitz, and P. W. Wiseman, "STICCS reveals matrix-dependent adhesion slipping and gripping in migrating cells," *Biophys. J.* **103**, 1672–1682 (2012).
29. M. A. Digman, P. W. Wiseman, A. R. Horwitz, and E. Gratton, "Detecting protein complexes in living cells from laser scanning confocal image sequences by the cross correlation raster image spectroscopy method," *Biophys. J.* **96**, 707–716 (2009).
30. A. P. Singh, J. W. Krieger, J. Buchholz, E. Charbon, J. Langowski, and T. Wohland, "The performance of 2D array detectors for light sheet based fluorescence correlation spectroscopy," *Opt. Express* **21**, 8652–8668 (2013).
31. J. Sankaran, X. Shi, L. Ho, E. Stelzer, and T. Wohland, "ImFCS: A software for imaging FCS data analysis and visualization," *Opt. Express* **18**, 25468–25481 (2010). Available at http://staff.science.nus.edu.sg/~chmw/~/resources/imfcs_software.html.
32. L. C. Hwang and T. Wohland, "Single wavelength excitation fluorescence cross-correlation spectroscopy with spectrally similar fluorophores: Resolution for binding studies," *J. Chem. Phys.* **122**, 114708 (2005).
33. P. Liu, T. Sudhakaran, R. M. Koh, L. C. Hwang, S. Ahmed, I. N. Maruyama, and T. Wohland, "Investigation of

- the dimerization of proteins from the epidermal growth factor receptor family by single wavelength fluorescence cross-correlation spectroscopy," *Biophys. J.* **93**, 684–698 (2007).
34. J. Buchholz, J. W. Krieger, G. Mocsár, B. Kreith, E. Charbon, G. Vámosi, U. Kebschull, and J. Langowski, "Fpga implementation of a 32x32 autocorrelator array for analysis of fast image series," *Opt. Express* **20**, 17767–17782 (2012).
 35. D. W. Marquardt, "An algorithm for least-squares estimation of nonlinear parameters," *J. Soc. Ind. Appl. Math.* **11**, 431–441 (1963).
 36. K. Levenberg, "A method for the solution of certain nonlinear problems in least squares," *Quart. Appl. Math.* **2**, 164–168 (1944).
 37. J. Wuttke, "lmfit 3.2 – a c/c++ routine for levenberg-marquardt minimization with wrapper for least-squares curve fitting, based on work by B.S. Garbow, K.E. Hillstrom, J.J. Moré, and S. Moshier, available at <http://apps.jens.fz-juelich.de/doku/sc/lmfit>," (2010).
 38. A. Corana, M. Marchesi, C. Martini, and S. Ridella, "Minimizing multimodal functions of continuous variables with the 'simulated annealing' algorithm corrigenda for this article is available here," *ACM T. Math. Software* **13**, 262–280 (1987).
 39. Y. H. Foo, N. Naredi-Rainer, D. C. Lamb, S. Ahmed, and T. Wohland, "Factors affecting the quantification of biomolecular interactions by fluorescence cross-correlation spectroscopy," *Biophys. J.* **102**, 1174–1183 (2012).
 40. QuickFit 3.0 can be downloaded free of charge from <http://www.dkfz.de/Macromol/quickfit/>.
 41. K. Greger, J. Swoger, and E. H. K. Stelzer, "Basic building units and properties of a fluorescence single plane illumination microscope," *Rev. Sci. Instrum.* **78**, 023705 (2007).
 42. A. Edelstein, N. Amodaj, K. Hoover, R. Vale, and N. Stuurman, "Computer control of microscopes using μ Manager," *Curr. Protoc. Mol. Biol.* **14**, 1–14 (2010).
 43. E. M. M. Manders, F. J. Verbeek, and J. A. Aten, "Measurement of co-localization of objects in dual-colour confocal images," *J. Microsc.* **169**, 375–382 (1993).
 44. The matlab scripts for the bead scan evaluation is freely available at: <http://www.dkfz.de/Macromol/quickfit/beadscan.html>.
 45. N. Bag, J. Sankaran, A. Paul, R. S. Kraut, and T. Wohland, "Calibration and limits of camera-based fluorescence correlation spectroscopy: A supported lipid bilayer study," *ChemPhysChem* **13**, 2784–2794 (2012).
 46. T. Wocjan, J. Krieger, O. Krichevsky, and J. Langowski, "Dynamics of a fluorophore attached to superhelical DNA: Fcs experiments simulated by brownian dynamics," *Phys. Chem. Chem. Phys.* **11**, 10671–10681 (2009).
 47. C.-H. Huang, "Phosphatidylcholine vesicles. formation and physical characteristics," *Biochemistry* **8**, 344–352 (1969). PMID: 5777332.
 48. L. A. Maguire, H. Zhang, and P. A. Shamlou, "Preparation of small unilamellar vesicles (SUV) and biophysical characterization of their complexes with poly-l-lysine-condensed plasmid DNA," *Biotechnol Appl. Biochem.* **37**, 73–81 (2003).
 49. J. Sankaran, N. Bag, R. S. Kraut, and T. Wohland, "Accuracy and precision in camera-based fluorescence correlation spectroscopy measurements," *Anal. Chem.* **85**, 3948–3954 (2013).
 50. M. Wachsmuth, "Fluoreszenzfluktationsmikroskopie: Entwicklung eines prototyps, theorie und messung der beweglichkeit von biomolekülen im zellkern," Ph.D. thesis, Ruprecht-Karls-Universität ,Heidelberg. (2001).
 51. J. R. Unruh and E. Gratton, "Analysis of molecular concentration and brightness from fluorescence fluctuation data with an electron multiplied ccd camera," *Biophys. J.* **95**, 5385–5398 (2008).
 52. N. Baudendistel, G. Müller, W. Waldeck, P. Angel, and J. Langowski, "Two-hybrid fluorescence cross-correlation spectroscopy detects protein–protein interactions in vivo," *ChemPhysChem* **6**, 984–990 (2005).
 53. G. Vámosi, N. Baudendistel, C.-W. von der Lieth, N. Szalóki, G. Mocsár, G. Müller, P. Brázda, W. Waldeck, S. Damjanovich, J. Langowski, and K. Tóth, "Conformation of the c-Fos/c-Jun complex in vivo: A combined FRET, FCCS, and MD-modeling study," *Biophys. J.* **94**, 2859–2868 (2008).
 54. B. K. Müller, E. Zaychikov, C. Bräuchle, and D. C. Lamb, "Pulsed interleaved excitation," *Biophys. J.* **89**, 3508–3522 (2005).
 55. A. N. Kapanidis, T. A. Laurence, N. K. Lee, E. Margeat, X. Kong, and S. Weiss, "Alternating-laser excitation of single molecules," *Acc. Chem. Res.* **38**, 523–533 (2005).
 56. J. Roszik, D. Lisboa, J. Szöllösi, and G. Vereb, "Evaluation of intensity-based ratiometric FRET in image cytometry—approaches and a software solution," *Cytometry A* **75A**, 761–767 (2009).
 57. S. Talwar, A. Kumar, M. Rao, G. I. Menon, and G. V. Shivashankar, "Correlated spatio-temporal fluctuations in chromatin compaction states characterize stem cells," *Biophys. J.* **104**, 553–564 (2013).
 58. S. Burri, D. Stucki, Y. Maruyama, C. Bruschini, E. Charbon, and F. Regazzoni, "Jailbreak imagers: Transforming a single-photon image sensor into a true random number generator," in "International Image Sensor Workshop," (2013). Snowbird, June 2013, available online http://www.imagesensors.org/PastWorkshops/2013Workshop/2013Papers/07-20_099-regazzoni_paper_revised.pdf.

1. Introduction

Fluorescence correlation spectroscopy (FCS) [1, 2] is a powerful experimental technique to measure the dynamics of fluorescently labeled molecules in solution and inside living cells [3]. It reports on the particle number, the diffusion coefficient, flow speeds, as well as photo-physical and chemical reaction rates by performing an autocorrelation analysis of the fluorescence intensity fluctuations measured inside a small observation volume (typically $10^{-15} \text{ l} = 1 \mu\text{m}^3$). FCS was extended to fluorescence cross-correlation spectroscopy (FCCS) to evaluate the cross-correlation between two or more separate color channels [4–9]. This allows to additionally extract information about the interaction between differently labeled particles. For an overview of the existing FCS/FCCS-techniques, see e.g. [10–12]. Both methods have found widespread application in confocal microscopes which measure one or a few measurement positions at a time. FCS has been extended to an imaging method, first by consecutive single-spot measurements [13], by line- [14] and circle-scanning [15], by line-confocal detection [8, 16], by spinning-disk microscopy [17], by multi-confocal detection [18, 19] and, in recent years, on total internal reflection (TIRF) [20] and SPIM microscopes [21, 22]. In the *supplementary information* (SI [23]) we present typical exemplary SPIM-FCS measurements, viz., organic dye in buffer, fixed GUVs, and fluorescent proteins in live cells (Fig. S11) to show the range of samples, to which the method is applicable. FCCS has been implemented for a small number of pixels on a two-focus two-color confocal setup [24], and with a line-scanning microscope for a few spatially separated pixels [25, 26]. It has been shown to work with low temporal resolution ($\sim 30 \text{ ms}$) as image cross-correlation spectroscopy [27] and, when averaging over larger subregions, as spatio-temporal image cross-correlation spectroscopy [28]. Raster image cross-correlation spectroscopy [29] uses the different time-scales embedded in a laser-scanning confocal image, to improve the temporal resolution, but at the cost of spatial resolution. However, all these methods either average over larger subregions in the acquired images or are in other ways (acquisition speed, z -sectioning) limited by the used microscopy techniques. To overcome these limitations, we extend FCCS into a fast and true imaging mode by using single plane illumination microscopy (SPIM-FCCS) with a high-speed electron-multiplying charge coupled device (EMCCD) camera, giving moderate to high temporal resolution ($0.3 - 1.0 \text{ ms}$) and good z -sectioning.

Similar to SPIM-FCS, SPIM-FCCS excites a single plane (thickness $\sim 1.3 \mu\text{m}$) in a sample. The difference in SPIM-FCCS is that two light sheets of different wavelength are used simultaneously to excite different fluorophores for the cross-correlation analysis. For detection we use an image splitter optics to separate the full spectral range into two distinct color channels which are imaged onto the same EMCCD camera. This sensor has been chosen due to its relatively high temporal resolution and high detection efficiency (quantum efficiency $> 95\%$). The properties of several other possible detectors have recently been studied and compared in [30], but EMCCD cameras currently offer the best compromise between acquisition speed and photosensitivity.

Here we show that SPIM-FCCS works on a range of simple calibration samples (organic dyes, labeled DNAs, microspheres, small unilamellar vesicles) and is applicable in live-cell measurements in the cytoplasm, nucleus and the membrane. In addition to the optical setup for SPIM-FCCS measurements, we describe its alignment and calibration in detail, and present a comprehensive theoretical framework and fit procedures for camera-based SPIM-FCCS. We especially discuss one- and two-component normal diffusion of two differently colored species A and B and their dimer AB.

2. SPIM-FCCS: The method

2.1. Introduction to SPIM-FCCS

In fluorescence fluctuation microscopy, the motion properties of fluorescently labeled particles are extracted from an analysis of the fluorescence fluctuations emitted at different positions in the sample. For FCCS measurements, the fluorescence signal emitted by each spot \vec{r} of a sample is split spectrally into a green color channel signal $I_g(t; \vec{r})$ and red signal $I_r(t; \vec{r})$. Then the normalized correlation functions (with $\gamma\rho \in \{gg, rr, gr, rg\}$)

$$g_{\gamma\rho}(\tau; \vec{r}) = \frac{\langle I_\gamma(t; \vec{r}) \cdot I_\rho(t + \tau; \vec{r}) \rangle}{\langle I_\gamma(t; \vec{r}) \rangle \cdot \langle I_\rho(t; \vec{r}) \rangle} - 1 = \frac{G_{\gamma\rho}(\tau)}{\langle I_\gamma(t; \vec{r}) \rangle \cdot \langle I_\rho(t; \vec{r}) \rangle} \quad (1)$$

are calculated. Here $\langle \cdot \rangle$ denotes a temporal average and $G_{\gamma\rho}(\tau) = \langle \delta I_\gamma(t) \cdot \delta I_\rho(t + \tau) \rangle$ is the non-normalized correlation function between the fluorescence fluctuations $\delta I_\gamma(t) = I_\gamma(t) - \langle I_\gamma \rangle$ in channels γ and ρ respectively. The autocorrelations $g_{gg}(\tau; \vec{r})$ and $g_{rr}(\tau; \vec{r})$ mainly contain information about the diffusion coefficient and concentration of the different labeled particles, while the amplitude of the cross-correlation $g_{gr}(\tau; \vec{r})$ reports on their interaction. As we will not use spatial cross-correlations between different points in the sample, we will omit the parameter \vec{r} from this point on. If theoretical models are known for the measured correlation functions, a parameter fit can yield parameters describing the mobility and interaction of the observed species.

To extend FCCS, which is most often implemented on point-scanning confocal microscopes to an imaging technology, we implemented it on a single plane illumination microscope (SPIM). The microscope was optimized for single-cell measurements with green and red fluorescent proteins (FP), using a blue and a green, $\sim 1.3 \mu\text{m}$ thin light sheet to excite fluorescence in only a fine slice of the cell. The detected light is imaged as two separate color channels onto a high-speed EMCCD camera (see Fig. 1(A)), and the cross-correlation between two color channels can be performed by cross-correlating the corresponding pixels time series. The optics have to be carefully aligned to ensure that the two cross-correlated pixels correspond to the same volume inside the sample (see section 3.2 for details on the alignment procedure).

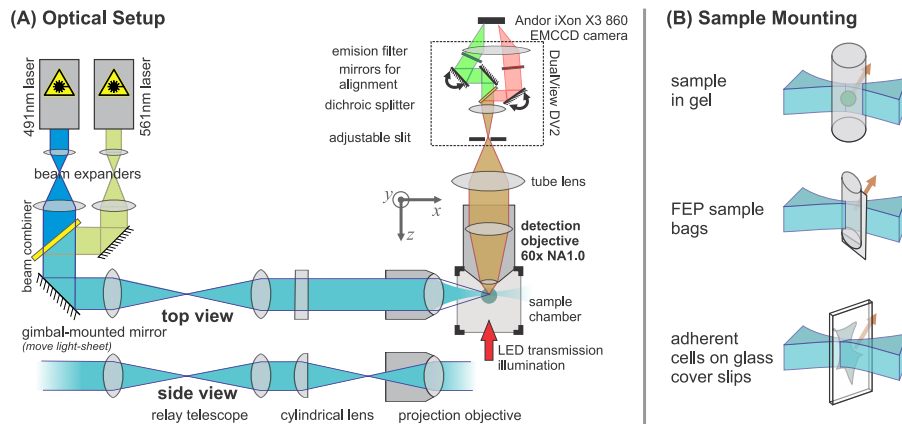


Fig. 1. Schematic view of the SPIMs described in this article: (A) shows the detailed optical setup and (B) shows three possible sample mounting schemes: Solid samples (e.g. beads for calibration) can be embedded in a gel cylinder, liquid samples are sealed into small thermoplastic bags and adherent cells are grown onto small glass pieces.

In this section, we will first derive the theoretical models required to extract information from the measured correlation functions. Then we give a short explanation of the full data evaluation pipeline that uses these models. An extended derivation and further comments can be found in the SI [23].

2.2. SPIM-FCCS models

Extending our previous work [21, 30, 31], we derive theoretical models for SPIM-FCCS and the simple situation of a bimolecular binding reaction $A + B \rightleftharpoons AB$. Our models allow us to determine the diffusion coefficients D_A , D_B and D_{AB} , as well as the concentrations c_A , c_B and c_{AB} of three molecular species A, B and AB present in this process. In a typical experiment, A and B are the green and red labeled monomers, whereas AB represents the double-labeled dimer formed from A and B.

To derive the FCCS correlation functions, we follow the same approach as in [25, 32, 33] and start from the fluorescence intensities $I_g(t)$, $\delta I_g(t)$ in the green and $I_r(t)$, $\delta I_r(t)$ in the red color channel. These can be written for any color channel γ and the set of molecular species $\mathbb{S} = \{A, B, AB, \dots\}$ as:

$$I_\gamma(t) = \int_{-\infty}^{\infty} \text{MDE}_\gamma(\vec{r}) \cdot \sum_{\chi \in \mathbb{S}} \eta_\gamma^\chi c_\chi(t, \vec{r}) dV, \quad \delta I_\gamma(t) = \int_{-\infty}^{\infty} \text{MDE}_\gamma(\vec{r}) \cdot \sum_{\chi \in \mathbb{S}} \eta_\gamma^\chi \delta c_\chi(t, \vec{r}) dV \quad (2)$$

Here η_γ^χ represents the molar fluorescence brightness of the fluorescent species χ in channel γ . The symbol $c_\chi(t, \vec{r})$ denotes the local particle concentration of species χ at time t and position \vec{r} and $\text{MDE}_\gamma(\vec{r})$ is the molecular detection efficiency of channel γ for an emitting particle at position \vec{r} . The fluorescence fluctuations $\delta I_\gamma(t)$ are calculated from the concentration fluctuations $\delta c_\chi(t, \vec{r})$.

For SPIM-FCS/FCCS we assume the same MDE as in our previous publications [21, 30, 31], i.e. a laterally constant Gaussian light sheet $I_{\text{LS}}(z) = \exp(-2z^2/w_{\text{LS}}^2)$ with $1/e^2$ -halfwidth w_{LS} for illumination, a pixel detector with square pixels (side length a) and a point spread function (PSF), that describes the imaging properties of the detection optics. The overall MDE is then calculated by an integral over the volume sampled by each point on the pixels ($\vec{r} = (x, y, z)^T$):

$$\text{MDE}_\gamma(\vec{r}) = \text{MDE}_\gamma(x, y, z) = \frac{1}{\mathcal{N}} \cdot I_{\text{LS}}(z) \cdot \int_0^a \int_0^a \text{PSF}_\gamma(x - \mu, y - \nu, z) d\nu d\mu, \quad (3)$$

where $\text{PSF}_\gamma(x, y, z) = \exp[-2 \cdot (x^2 + y^2)/w_\gamma^2 - 2z^2/z_\gamma^2]$ is the Gaussian point spread function of the detection objective. The factor \mathcal{N}^{-1} is a normalization constant, set to fulfill $\int_{-\infty}^{\infty} \text{MDE}_\gamma(\vec{r}) dV = 1$. Using these definitions, the correlation function Eq. (1) can be written as:

$$g_{\gamma\rho}(\tau) = \frac{\sum_{\chi \in \mathbb{S}} \eta_\gamma^\chi \eta_\rho^\chi \cdot G_{\gamma\rho}^\chi(\tau)}{\left(\sum_{\chi \in \mathbb{S}} \eta_\gamma^\chi \cdot c_\chi \right) \cdot \left(\sum_{\chi \in \mathbb{S}} \eta_\rho^\chi \cdot c_\chi \right)}. \quad (4)$$

where the $G_{\gamma\rho}^\chi(\tau)$ are factors describing the non-normalized (cross-)correlation functions of species χ between channels γ and ρ (Note: we defined $G_{\gamma\rho}^\chi(\tau)$ in such a way that its units are $1/\text{Length}^6$):

$$G_{\gamma\rho}^\chi(\tau) = \frac{\langle \delta I_\gamma(t) \cdot \delta I_\rho(t + \tau) \rangle}{\eta_\gamma^\chi \eta_\rho^\chi} = c_\chi \cdot \int_{-\infty}^{\infty} \int_{-\infty}^{\infty} \text{MDE}_\gamma(\vec{r}) \cdot \text{MDE}_\rho(\vec{r}') \cdot \phi_\chi(\vec{r}, \vec{r}', \tau) dV dV'. \quad (5)$$

To describe the diffusive motion of species χ , we use a Green's function of the following form:

$$\phi_\chi(\vec{r}, \vec{r}', \tau) = \frac{1}{(4\pi \cdot D_\chi \tau)^{3/2}} \cdot \exp\left[-\frac{(\vec{r} - \vec{r}')^2}{4D_\chi \tau}\right] \quad (6)$$

The integrals in Eq. (5) can be separated into three directional components $G_{\gamma\rho}^\chi(\tau) = c_\chi \cdot G_{\gamma\rho;x}^\chi(\tau) \cdot G_{\gamma\rho;y}^\chi(\tau) \cdot G_{\gamma\rho;z}^\chi(\tau)$. Each of these can be solved analytically:

$$G_{\gamma\rho;x}^\chi(\tau) = G_{\gamma\rho;y}^\chi(\tau) = \frac{1}{a} \cdot \left\{ \operatorname{erf}\left(\frac{\sqrt{2} \cdot a}{\sqrt{8D_\chi \tau + w_\gamma^2 + w_\rho^2}}\right) + \frac{\sqrt{8D_\chi \tau + w_\gamma^2 + w_\rho^2}}{a \cdot \sqrt{2\pi}} \cdot \left[e^{-\frac{2a^2}{8D_\chi \tau + w_\gamma^2 + w_\rho^2}} - 1 \right] \right\} \quad (7)$$

$$G_{\gamma\rho;z}^\chi(\tau) = \frac{\sqrt{2/\pi}}{\sqrt{8D_\chi \tau + z_\gamma^2 + z_\rho^2}}. \quad (8)$$

Here we assumed that no shift exists between the green and the red MDE ($\delta x = \delta y = \delta z = 0$), which was well achieved during the measurements for this paper, as shown in sections 3.2 and 3.3. The full correlation function including a non-zero shift and a possible directed flow, is provided in the SI [23]. In the case of 2-dimensional diffusion, one of the factors $G_{\gamma\rho;y}^\chi(\tau)$ or $G_{\gamma\rho;z}^\chi(\tau)$ is omitted (depending on the orientation of the 2D motion), e. g. for 2D-diffusion in the xz -plane, we separated the integrals in Eq. (5) only into two factors $G_{\gamma\rho}^\chi(\tau) = c_\chi \cdot G_{\gamma\rho;x}^\chi(\tau) \cdot G_{\gamma\rho;z}^\chi(\tau)$. Note that the concentrations are then in units of particles per area. This case is observed later in this paper, where the light sheets perpendicularly slices through the cell membrane (see SI [23], Fig. S10 for a sketch).

To further simplify the set of correlation functions in Eq. (4), we assume that the spectral properties of the two fluorophores A and B do not change on binding. Then the molar brightnesses η_γ^χ of species χ in channel γ can be written in terms of the molar channel brightness η_g of fluorophore A in the green channel and η_r of the fluorophore B in the red channel:

$$\begin{array}{lll} \eta_g^A & \equiv & \eta_g \\ \eta_r^A & = & \kappa_{gr} \eta_g \end{array} \quad \begin{array}{lll} \eta_g^B & = & 0 \\ \eta_r^B & \equiv & \eta_r \end{array} \quad \begin{array}{lll} \eta_g^{AB} & = & \eta_g \\ \eta_r^{AB} & = & \eta_r + \kappa_{gr} \eta_g. \end{array} \quad (9)$$

Here κ_{gr} is the crosstalk factor of the green into the red channel and we assume that there is no crosstalk of the red into the green channel, which is well justified for our dual-wavelength FCCS setup. The factors η_g and η_r can be estimated from the measured and background corrected average fluorescence intensities $\langle I_g(t) \rangle$ and $\langle I_r(t) \rangle$, as

$$\eta_g = \frac{\langle I_g(t) \rangle}{c_A + c_{AB}}, \quad \eta_r = \frac{\langle I_r(t) \rangle - \kappa_{gr} \cdot \langle I_g(t) \rangle}{c_B + c_{AB}}, \quad (10)$$

where the crosstalk coefficient κ_{gr} is determined in an A-only (green-only) sample as $\kappa_{gr} = \langle I_r(t) \rangle / \langle I_g(t) \rangle$. Note that we only used molar brightnesses $\eta_\gamma, \eta_\gamma^\chi$ in units of $1/(\text{particles}/\text{volume}) = \text{volume}$. Molecular brightnesses can be calculated as $\eta_\gamma^\chi / V_{\text{eff}}$, using the effective volume $V_{\text{eff}} := (\int \text{MDE}(\vec{r}) dV)^2 / \int \text{MDE}^2(\vec{r}) dV$.

The final system of correlation functions reads:

$$g_{gg}(\tau) = \frac{\eta_g^2 G_{gg}^A(\tau) + \eta_g^2 G_{gg}^{AB}(\tau)}{\eta_g^2 \cdot (c_A + c_{AB})^2} \quad (11)$$

$$g_{rr}(\tau) = \frac{\eta_r^2 \cdot [G_{rr}^B(\tau) + G_{rr}^{AB}(\tau)] + \kappa_{gr}^2 \eta_g^2 \cdot [G_{gg}^A(\tau) + G_{gg}^{AB}(\tau)] + 2\kappa_{gr} \eta_r \eta_g G_{gr}^{AB}(\tau)}{(\kappa_{gr} \eta_g c_A + (\eta_r + \kappa_{gr} \eta_g) \cdot c_{AB} + \eta_r c_B)^2} \quad (12)$$

$$g_{gr}(\tau) = g_{rg}(\tau) = \frac{\eta_g \eta_r G_{gr}^{AB}(\tau) + \kappa_{gr} \eta_g \eta_r G_{gr}^A(\tau) + \kappa_{gr} \eta_g^2 \cdot G_{gg}^{AB}(\tau)}{(\eta_g c_A + \eta_g c_{AB}) \cdot (\kappa_{gr} \eta_g c_A + (\eta_r + \kappa_{gr} \eta_g) c_{AB} + \eta_r c_B)} \quad (13)$$

We implemented these models in our data evaluation software QuickFit 3.0 and tested the implementation using different simulations, as described in the SI [23] and section 3.3.

From the concentrations c_A , c_B and c_{AB} , the amount of binding (as relative dimer concentration) can be calculated:

$$p_{AB} = \frac{c_{AB}}{\min(c_A, c_B)} \quad (14)$$

More general, the amount of cross-correlation (also a measure of binding) can also be defined from the correlation function amplitudes without assuming any concentrations:

$$q = \frac{g_{gr}(\tau_{\min})}{\min[g_{gg}(\tau_{\min}), g_{rr}(\tau_{\min})]}, \quad (15)$$

where $g_{\gamma\rho}(\tau)$ are either directly measured correlation functions (then τ_{\min} is the minimum lag time) or fitted model functions (then $\tau_{\min} = 0$).

2.3. Data evaluation

Several aspects of data processing for SPIM-FCS measurements have already been described [21, 22, 30, 31, 34]. We slightly modified these methods to yield the two-color cross-correlation functions. A schematic of all evaluation steps is shown in Fig. 2. Initially we acquire a time-series $\tilde{I}(t; \vec{r})$ of the sample with $5 \cdot 10^4 - 5 \cdot 10^5$ frames at a frame rate above 1000 frames per second (fps) using both lasers for illumination. In addition a short (~ 2000 frames) background series $B(t; \vec{r})$ without light sheet illumination is recorded with the same camera settings. Then

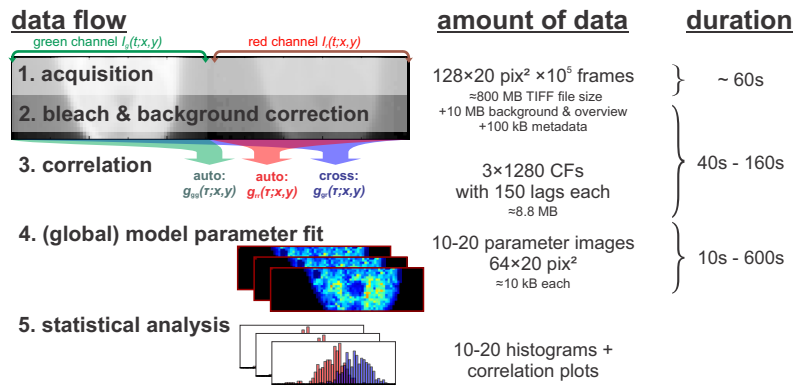


Fig. 2. FCCS data evaluation chain. The left column shows the progression from the raw input data to the statistically analyzed results. The right column gives typical numbers for the size of the dataset in each step.

the data is preprocessed by subtracting the averaged background ($\langle \tilde{I}(t; \vec{r}) \rangle - \langle B(t; \vec{r}) \rangle$), splitting the images series into two color channels and computing the auto- and cross-correlation functions using multi- τ -algorithm. If necessary a bleach correction is performed independently for every pixel, by fitting e. g. an exponential decay (or a more complex function) to the time-series in each pixel and then detrending the initial time-series, while preserving its ideal average and variance, as described in [14]. We checked this correction method using SPIM-FCS simulations of a depleting reservoir, which show that the obtained mobility parameters are not altered by the correction. Details on the correction method and the simulation results can be found in the SI [23].

Finally the model functions $g_{\gamma\rho}(\tau; c_A, c_{AB}, D_A, D_{AB}, \dots)$, derived in the last section are fitted to the experimental curves ($\tau_i, \hat{g}_{gg,i}, \hat{g}_{gr,i}, \dots$), measured at discrete lag times τ_i . We choose a global fitting method that simultaneously minimizes the least-squares deviations of the fit functions from the measurements. The optimal parameter vector $\vec{\beta}$ is then the solution of this least-squares optimization problem:

$$\vec{\beta}^* = \arg \min_{\vec{\beta}} \sum_{\gamma\rho=\{gg,rr,gr,rg\}} \sum_i \left[\frac{\hat{g}_{\gamma\rho,i} - g_{\gamma\rho}(\tau_i; \vec{\pi}_{\gamma\rho}(\vec{\beta}))}{\hat{\sigma}_{\gamma\rho,i}} \right]^2, \quad (16)$$

where $\vec{\pi}_{\gamma\rho}(\vec{\beta})$ maps the “global” parameter vector $\vec{\beta}$ to the “local” vector containing only the parameters used by the model function $g_{\gamma\rho}(\cdot; \cdot)$. To solve this optimization problem we used either a version of the Levenberg-Marquardt algorithm [35, 36], implemented in the software library lmfit [37] or our own implementation of the simulated annealing stochastic optimizer [38].

Each global fit incorporates the two autocorrelation and the cross-correlation functions from each pixel. The concentrations c_A , c_B and c_{AB} are always linked over these three correlation curves. In simple cases, where only one diffusing component is visible in the correlation functions, also the diffusion coefficients D_A , D_B and D_{AB} are linked in the same manner. In more complex cases, where two diffusing fractions per species are required to describe the data, we found that the models do no longer converge reliably and with physically meaningful fit parameter values. So we simplified Eq. (11)-Eq. (13), by assuming two diffusing components per channel which were no longer assigned to any specific species.

$$g_{gg}(\tau) = \frac{\eta_g^2 c_A + \eta_g^2 c_{AB}}{\eta_g^2 \cdot (c_A + c_{AB})^2} \cdot \check{G}_{gg}^G(\tau) \quad (17)$$

$$g_{rr}(\tau) = \frac{\eta_r^2 \cdot [c_B + c_{AB}] + \kappa_{gr}^2 \eta_g^2 \cdot [c_A + c_{AB}] + 2\kappa_{gr}\eta_r\eta_g c_{AB}}{(\kappa_{gr}\eta_g c_A + (\eta_r + \kappa_{gr}\eta_g) \cdot c_{AB} + \eta_r c_B)^2} \cdot \check{G}_{rr}^R(\tau) \quad (18)$$

$$g_{gr}(\tau) = g_{rg}(\tau) = \frac{\eta_g \eta_r c_{AB} + \kappa_{gr} \eta_g \eta_r c_A + \kappa_{gr} \eta_g^2 \cdot c_{AB}}{(\eta_g c_A + \eta_g c_{AB}) \cdot (\kappa_{gr} \eta_g c_A + (\eta_r + \kappa_{gr} \eta_g) c_{AB} + \eta_r c_B)} \cdot \check{G}_{gr}^{GR}(\tau), \quad (19)$$

where the correlation functions are defined using Eq. (7) and Eq. (8) as $\check{G}_{\gamma\rho}^X(\tau) \equiv G_{\gamma\rho;x}^X(\tau) \cdot G_{\gamma\rho;y}^X(\tau) \cdot G_{\gamma\rho;z}^X(\tau)$. The concentrations were still linked. This approach then resembles the analysis performed in [33, 39], where each curve was fitted separately and finally the amplitudes were analyzed with a linked fit model.

The complete data processing and fitting pipeline is freely available in the software packages QuickFit 3.0 [40] and in parts in ImFCS [31]. Typical data processing times with QuickFit 3.0 on a modern computer (AMD Phenom II 1090T, 3 GHz, 16 GB RAM running Linux) are 40 – 120 s for background and bleach correction, as well as correlation of 100,000 frames with 128×20 pixels each. Model fitting can be done with ~ 50 fits/s for single curve fits and a

1-component diffusion model. Our global fitting strategy reaches 2.5 – 7 fits/s depending on the number of free parameters in the models. Detailed data is given in the SI [23].

3. Experimental setup

3.1. A light sheet microscope with dual color excitation and detection

We used two home-built SPIM microscopes situated in Heidelberg (SPIM1) and Singapore (SPIM2). Both instruments are comparable in their setup and performance. Here we only give an overview of the systems (see Fig. 1(A)). A detailed description can be found in the SI [23]. The basic setup of our type of SPIM is described in [41]. The microscopes are optimized to perform SPIM-FCS/FCCS in single live cells. The light sheets are typically $\sim 1.3 \mu\text{m}$ thick ($1/e^2$ -halfwidth) and the field of view is about $50 \times 50 \mu\text{m}^2$ at a pixels size of 400 nm. The detection volume defined by each pixel of the camera is about $V_{\text{eff}} = 2.5 - 3 \mu\text{m}^3$, as compared to $V_{\text{eff}} = 0.5 - 1 \mu\text{m}^3$ in a confocal microscope [30].

We extended the SPIM setup, as described in [41], with a dual-excitation beam path combining two lasers (a blue 491 nm and a green 561 nm solid-state laser) with two distinct beam expanders. This is necessary to compensate for the chromatic aberrations of the two laser light sheets. The laser beams are combined after expansion using a dichroic mirror. This allows both light sheets to be steered independently. A telescope relays the combined beams to the cylindrical lens, which forms the light sheet together with a microscope air objective (SPIM1: 10x/NA0.3, SPIM2: 20x/NA0.25). The light sheets are projected through No. 1.0 cover slips into the medium-filled (e.g. deionized water, or Hanks' buffer medium) sample chamber. The intensity in each light sheet was 50 – 100 W/cm² during all measurements, which is a factor of 10 – 30 below typical intensities used for confocal FCS in live cells ($\sim 1500 \text{ W/cm}^2$).

Fluorescence detection is performed using a 60x/NA1.0 water dipping objective and a corresponding tube lens. The fluorescence signal is then split with image splitter (DualView DV2, Photometrics, Tucson, USA) into two images projected side-by-side onto a 128×128 pixel high-speed EMCCD camera (iXon X3 860, Andor, Belfast). The temporal resolutions of measurements given throughout this manuscript are frame repetition times, i.e. the sum of the exposure time and the readout time. The latter was 60 μs for all measurements. Binning was always performed during the data processing step and not on the camera. As different filter sets were used for the measurements in this paper, the crosstalk κ_{gr} is given in the text where necessary. Generally the crosstalk for eGFP was between $\kappa_{\text{gr}} = 3.5\%$ and 9%, and for Alexa-488 between $\kappa_{\text{gr}} = 5.4\%$ and 11.8% (both depending on the used filter set). Note that all model fits in this paper already incorporate a correction for the respective crosstalk.

The samples are mounted on a motorized XYZ-translation stage, allowing to acquire 3D image stacks. In addition to the lasers a white light emitting diode (LED, W42182/U2, Seoul Semiconductor, Ansan-city, Gyeonggi-do, Korea) can be used for transmission illumination. All electronic devices (stages, cameras, lasers, LED, ...) are controlled by a central computer, which also performs the data acquisition. We use QuickFit 3.0 [40] as a control and acquisition software on SPIM1 and the Andor Solis software on SPIM2. The image series (including a background measurement without illumination) are stored as 16-bit uncompressed TIFF-files (tagged image file format) and could be written to hard disk in real-time. All data evaluation is then performed off-line (see section 2.3) using either QuickFit 3.0 or ImFCS.

3.2. Alignment procedure

As the focal overlap is a very important parameter for any FCCS data evaluation, special care has to be taken when aligning the instrument. The blue 491 nm laser is aligned first, while imaging its light sheet profile using a mirror under 45° to the light sheet propagation axis (see SI [23] and Ref. [30]). Then the green 561 nm is adjusted to overlay the blue laser as precisely

as possible. We routinely achieve a peak-peak distance between the blue and green light sheet, $\delta z < 100$ nm (at a typical light sheet width of ~ 1.3 μm).

In a second step the image splitter optics are aligned, by imaging an electron microscopy grid with 1500 or 2000 lines per inch (grid spacing: 16.9 μm or 12.7 μm respectively; Lotech Scientific Supply Pte. Ltd, Singapore) in transmission illumination mode. The overlap of the two color channels was optimized using a special live-view of the difference between the two half images in QuickFit 3.0 and then maximizing the image cross-correlation coefficient between them. It is also possible to use the open source software $\mu\text{Manager}$ [42] with its plugins “Split View” and “Co-localization” [43] for the same task.

Finally the alignment and focal volumes were checked with a z -scan of TetraSpec fluorescent micro-spheres (100 nm diameter, T7279 Microspheres, Life Technologies GmbH, Darmstadt, Germany) embedded in a gel cylinder (0.5% Phytigel, P8169, Sigma-Aldrich Chemie GmbH, Munich, Germany) supplemented with 0.1% MgSO_4 . A Matlab script (Matlab 2012a, MathWorks, Ismaning, Germany) was developed and used to fit a 3D Gaussian model function to each bead in both channels. This allowed us to measure the displacement of the MDEs in all directions (available online: [44]). We routinely reach a lateral and longitudinal displacement δx , δy and δz of better than 100 nm. In section 3.3 we show FCCS simulations which confirm that this displacement leads to a negligible ($< 5\%$) reduction of the measured relative concentrations. Exemplary results and detailed protocols are shown in the SI [23] section S7.

To complete the alignment, we routinely check the setup in a final step with in-vitro standard samples (e. g. TetraSpec beads from stock, different double-labeled double-stranded DNAs in TE buffer, details and example measurements, see section 4). With these measurements we could check again the overlap of the two color channels, as a good focal overlap results in a high cross-correlation amplitude. The data was also used to perform a daily calibration of the focal volumes. In contrast to confocal FCS/FCCS, we do not need a standard sample with known diffusion coefficient. The exactly known pixel size of the camera can be used as a ruler to independently determine the absolute diffusion coefficient [30, 45]. Calibration was done with several different samples for each color channel separately. All samples yield comparable results for the daily focal sizes w_g and w_r (z_g and z_r were taken from the bead or light sheet scan), which also stayed constant with a relative standard deviation of $\leq 10\%$ over a period of 9 months (data shown in SI [23], Fig. S8). Both instruments used for this paper yield slightly different, but still stable and consistent focal parameters. The setups are stable without realignment for continuous measurements over up to 24 hours. The focal parameters stayed constant within the errors over several months (data, see SI [23]).

3.3. Simulations on the error due to misalignment

A crucial part of the alignment procedure are the displacements δx , δy and δz between the green and red detection volume. We used FCCS simulations to determine a threshold for these, which allows to do measurements with a small to negligible error. We extended the simulation program described in Refs. [30, 34, 46] to allow FCCS measurements. In a first step, this program creates random walk trajectories of 700 – 900 particles in a simulational box (all with the same diffusion coefficient, overall particle concentration $c_{\text{all}} \approx 1$ nM). The particles carry green, red or both fluorophores in different proportions $c_{\text{DL}}/c_{\text{all}}$ ranging from single-label only ($c_{\text{DL}}/c_{\text{all}} = 0$) to double-label (DL) only ($c_{\text{DL}}/c_{\text{all}} = 1$). A blue and a green light sheet illuminate the walkers, and two detection volumes for the green and red color channels are set up. The focal parameters approximately match those of the actual SPIM-FCCS setups used for this paper. The distance between the volumes is varied in eleven steps between $\delta x = 0$ nm and $\delta x = 2000$ nm. Detailed simulation parameters are given in the SI [23].

For each combination of $c_{\text{DL}}/c_{\text{all}}$, shift δx and one of two realistic crosstalk coefficients

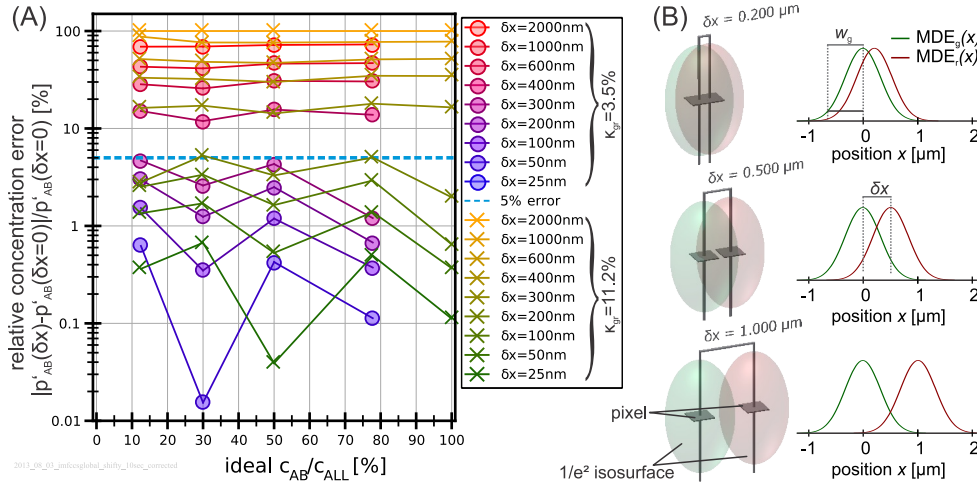


Fig. 3. Fit results when assuming no shift $\delta x = 0$ in the fit model, given that a shift $\delta x > 0$ actually is present in the microscope setup. (A) The graph shows the relative error, as defined by Eq. (21) at different crosstalk coefficients $\kappa \equiv \kappa_{gr}$ and focal shifts δx (colored green-orange or blue-red). the thick orange line marks an error level of 5% which is still acceptable. (B) depicts the simulated foci (as $1/e^2$ -isosurfaces) at different shifts δx . The camera pixels in the object space (pixel size $a = 400$ nm) are shown as gray squares inside the foci.

$\kappa_{gr} = 3.5\%$ and $\kappa_{gr} = 11.2\%$, the two autocorrelations and the cross-correlation curves were simulated and evaluated with a global fit to the SPIM-FCCS models described before. As in all measurements in this paper, we assumed $\delta x = \delta y = \delta z = 0$ for the fit. For each combination the fit yields a focus shift dependent relative concentration

$$p'_{AB}(\delta x) = \frac{c_{AB}(\delta x)}{c_{all}(\delta x)} = \frac{c_{AB}(\delta x)}{c_A(\delta x) + c_B(\delta x) + c_{AB}(\delta x)} \quad (20)$$

from which we estimated the relative error, when assuming $\delta x = 0$, instead of the actual $\delta x > 0$:

$$\text{err}(\delta x) = \frac{|p'_{AB}(\delta x) - p'_{AB}(0)|}{p'_{AB}(0)}. \quad (21)$$

Fig. 3 shows the results of these simulations. Further plots with example correlation functions and other representations of the results are given in the SI [23] (Fig. S16 – Fig. S18). The data shows that if we accept an error margin of $\text{err}(\delta x) < 5\%$, we can draw the conclusion that the instrument has to be aligned to $\delta x, \delta y, \delta z < \delta_{5\%} = 200$ nm. As shown in the last section 3.2, this is easily possible with the methods described there.

4. *In-vitro* samples

In this section we present several test measurements, to validate SPIM-FCCS. We first discuss possible samples for alignment. Then we compare SPIM-FCCS measurements with confocal FCCS experiments, on the same samples, to show that both methods yield the same results.

As test samples (for routine calibration and checking), we used either 100 nm diameter fluorescent microspheres (TetraSpec [T7279] Microspheres, Life Technologies GmbH, Darmstadt, Germany) directly from stock, or different double-stranded DNA samples (dsDNA), labeled

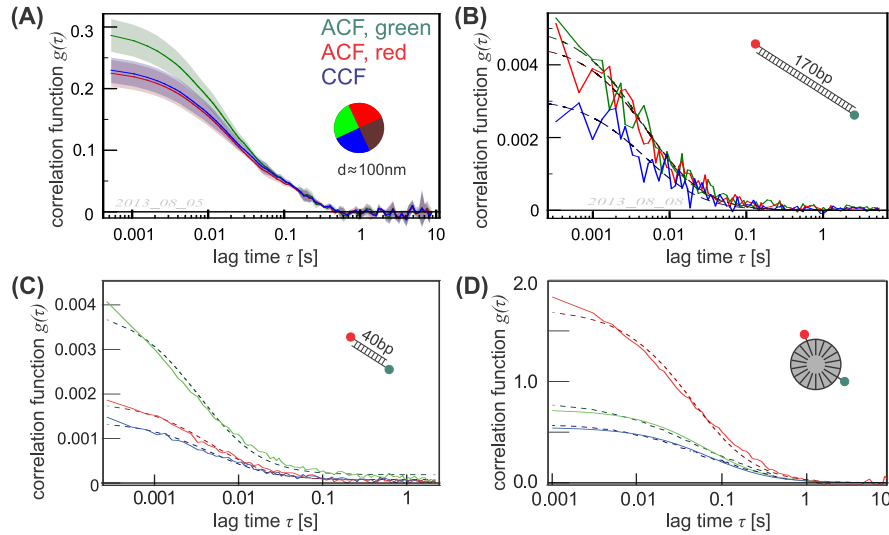


Fig. 4. Example auto- (green/red) and cross-correlation curves (blue) of FCCS standard samples: (A) TetraSpec beads [150,000 frames, 128×20 pixel, $\tau_{\min} = 0.53$ ms, 3 runs], (B) 170bp dsDNA [700,000 frames, 128×6 pixel, $\tau_{\min} = 0.29$ ms], (C) 40bp- dsDNA [100,000 frames, 128×4 pixel, $2 \times$ -binning, $\tau_{\min} = 0.27$ ms], (D) double labeled SUV [60,000 frames, $\tau_{\min} = 128 \times 20$ pixel, $\tau_{\min} = 1.04$ ms]. The graphs show the correlation functions of a single pixel and where available average and standard deviation over several runs. Dashed lines are fits to the data.

either with a single fluorophore or double-labeled with two different colors. The DNA samples were diluted in TE buffer (10 mM Tris, 0.1 mM Ethylenediaminetetraacetic acid, EDTA, pH 7.5) to the desired concentration. We used the 170 bp-long “601”-nucleosome binding sequence (fragment length: ~ 58 nm), labeled with an Alexa-488 and an Alexa-594 dye on opposite ends of the strand. Labeling was performed by amplifying the DNA sequence with two labeled primers using the polymerase chain reaction (PCR). Alternatively a short 40 bp double-labeled dsDNA-fragment (fragment length: ~ 13.6 nm) was used. As a third test sample that can be easily produced in any lab, we used small unilamellar vesicles (SUVs) with two spectrally distinct lipid dyes and prepared according to the protocol given in [23, 47, 48].

Example correlation curves of all these samples are shown in Fig. 4 and Tab. 1 summarizes typical numerical values. All measurements were carried out at room temperature (between 22°C and 25°C). We heat-sealed between $20 \mu\text{l}$ and $50 \mu\text{l}$ of each solution into plastic sample bags, as described elsewhere [30].

In addition to the calibrations above, we used a 607 bp dsDNA (fragment length: ~ 206 nm) to compare the performance of light sheet and confocal microscopy based FCCS. This DNA, was either labeled with Alexa-488, Alexa-594 or both dyes (on opposite ends of the strand) and mixed in different proportions. The same samples were measured on a confocal microscope (details on the setup, see SI [23] and Ref. [50]) and on our SPIM. Again we used 2×2 pixel binning to reduce the noise on the measured CFs, which were subsequently fitted with the SPIM-FCCS models described above, or the according confocal FCCS models (see SI [23]) using a global fit. Fig. 5 shows the results of these measurements (additional plots and example CFs are available in the SI [23], Fig. S12). There is a linear relation between the parameters measured with the two methods (as green [outlier-robust] regression lines in Fig. 5(A)), but the ideal slope 1 is not reached. The deviations from the ideal result can be explained by the

Table 1. Summary of typical diffusion coefficients recalculated to their value $D_{20,W}$ at 20°C in water and of the relative cross-correlation amplitudes q (not crosstalk-corrected) obtained with different samples. The diffusion coefficients of single dyes (Alexa-488, eGFP etc.), as typically measured in SPIM-FCS, are given for comparison.

Sample	$D_{20,W}[\mu\text{m}^2/\text{s}]$	$q[\%]$	Sample	$D_{20,W}[\mu\text{m}^2/\text{s}]$	$q[\%]$
40bp dsDNA	(36 ± 8)	(75 ± 10)	eGFP [†]	(66 ± 8)	—
170bp dsDNA*	(22 ± 3)	(59 ± 8)	Alexa-488 [†]	(232 ± 41)	—
607bp dsDNA*	(6.3 ± 0.9)	(46 ± 18)	Atto-565 [†]	(221 ± 100)	—
SUV	(6 ± 2)	(60 ± 8)	Alexa-594 [†]	(158 ± 96)	—
TetraSpec*	(3.1 ± 0.2)	(104 ± 8)			

* an average over 6 measurements during two week

[†] These particles are so fast, that the measured diffusion coefficients are not absolutely accurate, cf. [49]

noisiness of the SPIM-FCCS correlation functions (red crosses show the results without pixel binning) and the accompanying uncertainty in the fit results. Also imperfect background, bleach and crosstalk corrections may influence the results, leading to an offset at low dimer concentrations. The measured concentrations are about a factor of (9.5 ± 2.1) higher than the actual concentrations, or the concentrations measured in confocal FCS/FCCS. This fact was already discussed in Refs. [30, 51]. But, as especially the 607 bp DNA measurement shows, reasonable values for relative concentrations can still be extracted from SPIM-FCCS measurements. Also it shows that both microscopy methods yield comparable dynamic ranges for the relative dimer concentration. A calibration of the concentrations can be performed by measuring a dilution series of a standard sample (e. g. a mixture of single- and double-labeled DNA) with know absolute and relative concentrations. A possible protocol is given in the SI [23] and example results for our SPIM-FCCS setup in Fig. S21. Using the calibrated concentrations, also absolute values for e. g. a dimeric dissociation constant $K_D = c_A \cdot c_B / c_{AB}$ can estimated using SPIM-FCCS.

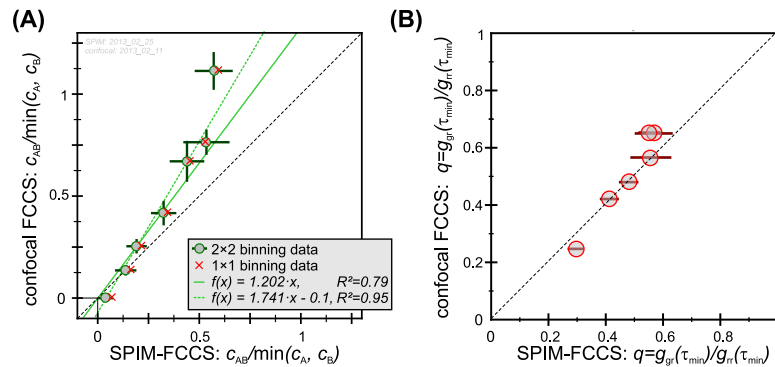


Fig. 5. Comparison between confocal and SPIM-FCCS measurements. (A) shows the relative dimer concentration p_{AB} and (B) the relative cross-correlation amplitude q . The black dashed line represents the ideal result (slope 1). Different mixtures of single- and double-labeled 607bp long dsDNA strands were measured on both instruments. For the SPIM, the acquisition setting were: 700,000 frames, 128×6 pixels, no binning (red crosses) or 2×2 pixel binning (green circles), $\tau_{\min} = 0.33$ ms. Data from the confocal measurements are average and standard deviation (SD) over 7 consecutive runs (30 s each). For SPIM they are average and SD over all pixels from 3 – 4 separate experiments. Green lines in (A) represent robust regressions to the 2x-binning data.

5. *In-vivo* measurements

5.1. Sample preparation

To establish the applicability of SPIM-FCCS in live-cell measurements, we transfected adherent mammalian cells with different vectors expressing fluorescent proteins in the cytoplasm, nucleoplasm and the cellular membrane.

For SPIM measurements, the cells were grown on small pieces (about $5 \times 10 \text{ mm}^2$) of No. 3 cover slips (0.28 mm – 0.32 mm thick, No. 16301, Neolab, Heidelberg, Germany) put into the culture dishes before seeding the cells. Before use, the glass pieces were thoroughly washed with acetone or 70% ethanol and deionized water, then sterilized. For the measurement, a glass cover slip was clamped into self-closing tweezers. Then it was mounted from above in the SPIM sample chamber, which was filled with Hanks' balanced salts solution (PAN-Biotech, Aidenbach, Germany). To avoid any direct reflection of the laser light to the sensor the glass cover slip was positioned under an angle below 45° with respect to the light sheet.

5.2. Proteins in the cyto- and nucleoplasm

HeLa cells were grown in phenol-red free medium as described above. They were transfected using FuGENE HD (Promega GmbH, Mannheim, Germany), one day after seeding. We used either a plasmid expressing an eGFP-mRFP1-dimer molecule or a plasmid expressing monomeric eGFP and mRFP1 separately (for details on the plasmids, see [52]). The proteins were located in the cytosol and nucleoplasm, see Fig. 6(D). Measurements were performed 24 – 36 h after transfection. For a detailed protocol, see the SI [23]. We acquired SPIM-FCCS measurements with typically 64×20 pixels per color channel at a temporal resolution of 0.53 ms and binned

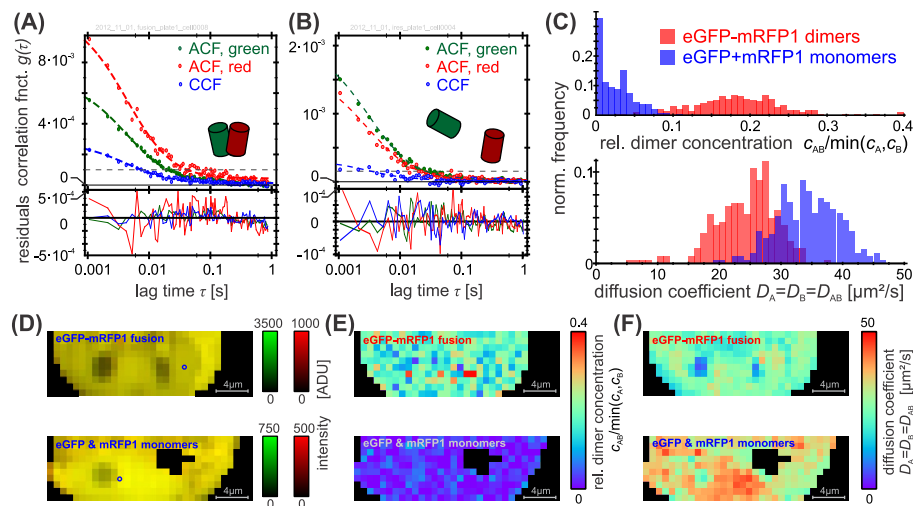


Fig. 6. SPIM-FCCS control measurement of eGFP-mRFP1-dimers and eGFP + mRFP1-monomers expressed in HeLa cells. (A) and (B) show example correlation functions and fits for the dimer and monomer sample, horizontal dashed lines are the level of cross-correlation explained by crosstalk (C) shows histograms of the relative dimer concentration p_{AB} and of the diffusion coefficient $D_A = D_B = D_{AB}$ in two exemplary cells. (D) shows intensity (blue circles mark position of CFs in A,B), (E) shows relative concentration images (same data as in C) and (F) shows the diffusion coefficient maps. The acquisition settings were: 128×20 pixel, 2×2 binning, 1.06 ms temporal resolution, 211 s measurement duration (200,000 frames) for the each cell.

2×2 pixels. The binning increases the correlation time and reduces noise on the CFs. Thus it improves the accuracy with which diffusion coefficients can be determined [49]. The EM-gain of the camera was set to 300 for all samples. As bleaching was not negligible, a bleach correction, using a mono-exponential ($f(t) = A \cdot \exp[-t/\tau_B]$) or modified mono-exponential model $f(t) = A \cdot \exp[-(t + f_2 t^2)/\tau_B]$ was used.

Data was fitted with a global 1-component SPIM-FCS model with only one diffusion coefficient for all species, i. e. $D_A = D_B = D_{AB}$. Fig. 6 displays example results of these measurements, showing a shift of the relative dimer concentration from $p_{AB} = (0.025 \pm 0.023)$ for the monomers to (0.18 ± 0.06) for eGFP-mRFP1-transfected cells. The models already contain an implicit crosstalk-correction. The non-corrected relative correlation amplitude averaged over several cells was $q = (0.46 \pm 0.07)$ for the dimers and (0.25 ± 0.04) for the monomers. These values are comparable to typical results from confocal FCCS experiments [52]. Note that our fusion construct shows $\sim 30\%$ Förster resonance energy transfer (FRET), due to its 7 amino acid short linker [53], which reduces the detectable cross-correlation amplitude [54].

The diffusion coefficient drops from $D_{\text{monomer}} = (34 \pm 5) \mu\text{m}^2/\text{s}$ for the monomers to $D_{\text{dimer}} = (25 \pm 5) \mu\text{m}^2/\text{s} \approx 0.74 \cdot D_{\text{monomer}}$ for the dimer, which is comparable to the values for eGFP monomers and dimers reported for confocal FCS/FCCS measurements in [13, 52].

5.3. Membrane-bound proteins

We tested the applicability of SPIM-FCCS to membrane-associated proteins using Chinese hamster ovary (CHO) cells expressing either the epidermal growth factor receptor (EGFR) labeled with eGFP and mRFP1 (eGFP-EGFR-mRFP1), or coexpressing the single fluorescent proteins fused to a plasma membrane targeting sequence (PMT-eGFP, PMT-mRFP1) from two different plasmids. The EGFR protein has a trans-membrane domain and the PMT sequence leads to an enrichment of the dyes in the cellular membrane. The EGFR construct serves as positive control whereas the PMT constructs should show no cross-correlation. All constructs have already been described and used for confocal single-wavelength FCCS in Ref. [33]. Measurements for these proteins were performed 48 – 60 h after transfection with FUGENE HD, as the expression of EGFR was too low after 24 – 36 h. Again we acquired SPIM-FCCS measurements with 64×20 pixels per color channel at a temporal resolution of 0.53 ms and an EM-gain of 300.

As small motions of the cellular membrane can interfere with the FCCS measurement, we selected only cells that showed negligible movement during the measurement and where the CFs $g_{\gamma\rho}(\tau)$ decayed to 0 for large lag times τ . We used a strong variant of the bleach correction, which fits a modified exponential function $f(t) = A \cdot \exp[-(t + f_2 t^2 + f_3 t^3)/\tau_B]$ to the data. Again a 2×2 pixel binning was used to improved CF statistics. This also reduces artifacts due to membrane motion, as the relation between motion and focus size is improved. Finally a 2-component SPIM-FCCS model for 2D diffusion in the xz -plane was fitted to the data. Only the concentrations were linked over all channels, whereas the diffusion coefficients and diffusing species fractions were specific to each channel. Fig. 7 shows exemplary results. From a larger set of measurements, distributed over several weeks, we get an average $p_{AB} = (0.36 \pm 0.20)$ for the PMT-cells and $p_{AB} = (0.93 \pm 0.62)$ for the EGFR samples. These numbers are average and standard deviation over 42 (PMT) and 33 (EGFR) single-cell average values (see SI [23], Fig. S14). The non-zero value of p_{AB} for the negative control (PMT-cells) can be explained by a non-perfect crosstalk correction and especially by remaining and non-corrected membrane motion. The results compare well to the curves and values reported in Ref. [33] from confocal single-wavelength FCCS.

Our data demonstrates that SPIM-FCCS measurements in membranes are possible and that we can reproduce the results obtained with confocal measurements in Ref. [33], if cells and

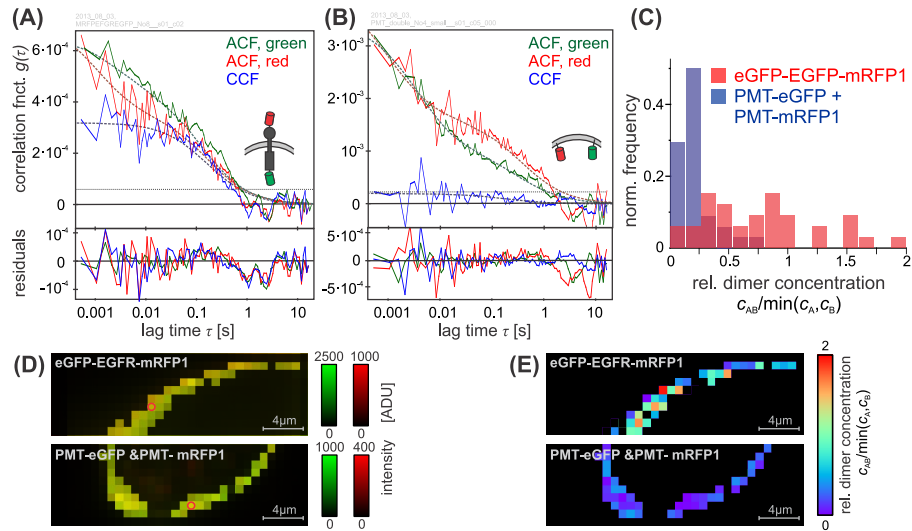


Fig. 7. SPIM-FCCS control measurement of eGFP-EGFR-mRFP1 and PMT-eGFP- + PMT-mRFP1-monomers expressed in CHO cells. (A) and (B) show example correlation functions and fits for the dimer and monomer sample, horizontal dashed lines are the level of cross-correlation explained by crosstalk (C) shows histograms of the relative dimer concentration p_{AB} , (D) shows intensity (red circles mark position of CFs in A,B), and (E) shows relative concentration images (same data as in C). The acquisition settings were: 128×20 pixel, 2×2 binning, 0.53 ms temporal resolution, 99 s measurement duration (100,000 frames) for the each cell.

pixels are selected carefully to exclude any artifacts due to movement of the cells. The SPIM illumination slices through the middle of the cell and therefore the membrane is only visible as a ring which limits the number of pixels in which membrane dynamics can be measured (thus the histogram in Fig. 7(C) has low resolution). It should be noted that TIRF imaging FCCS would provide a better solution if solely membrane dynamics are of interest, since then most pixels of the acquired image will show a part of the membrane. While SPIM-FCCS is a good choice if dynamics inside the cell and on the membrane need to be measured at the same time.

6. Conclusion

In this work we introduce single plane illumination microscopy based two-color fluorescence cross-correlation spectroscopy (SPIM-FCCS) as a method for *in-vitro* and *in-vivo* measurements. We used custom-built light sheet microscopes, which were equipped with a dual-color excitation. An image splitter was used to separately image the detected fluorescence into two separate color channels on a single EMCCD camera. Based on our previous work [21, 30, 31], we developed a comprehensive and extendable theoretical framework for camera-based SPIM-FCCS. With our setup, we can acquire 3804 auto- and cross-correlation functions (three functions for each of 128×20 pixels) within 53 s with good statistics in live cells. Data processing and fitting can be performed within less than 10 min per cell. For data fitting we use a global fit strategy which allows to extract the concentrations of each species in a mixture of single- (green or red) and double-labeled (green-red) molecules. We showed how a SPIM-FCCS setup can be aligned and which test samples can be used to check the alignment and the setup. Easily available samples are, for instance, multi-colored microspheres, which are readily available from several companies. Also several DNA constructs, which can be produced using PCR, are

a viable choice. As a third option we tested small unilamellar vesicles, which can be produced by following a simple protocol with good repeatability and uniform size distribution. We compared the performance of SPIM-FCCS and confocal microscopy based FCCS and could show that our new method yields the same results as the established technique.

Finally we applied SPIM-FCCS to live-cell measurements in the cytoplasm, nucleus and the cellular membrane. HeLa cells were transected with an eGFP-mRFP1-dimer as positive and the two fluorescent proteins separately as a negative control. These molecules are located in the cytoplasm as well as in the nucleus. To check the applicability to membrane-bound proteins, we transfected CHO cells with a double-labeled epidermal growth factor receptor (eGFP-EGFR-mRFP1) as positive or the single fluorescent proteins fused to a membrane targeting sequence (PMT-eGFP, PMT-mRFP1) as a negative control. With SPIM-FCCS we obtain the same results that have already been reported for these samples with confocal FCCS [33,52].

In summary light sheet based FCCS provides a robust and quantitative bio-imaging tool to understand the dynamics of bio-molecules in live cells. It allows one to measure spatially varying molecular interactions (as expected e. g. for transcription factors in the interphase nucleus). Compared to confocal microscopy based FCCS, imaging FCCS gives much better statistics per cell, as hundreds of points are measured in parallel. Using a calibration standard, this method will also allow to quantitatively measure spatially varying equilibrium constants *in-vitro* and in living cells. The technique can easily be extended with fast, frame-based alternating of the excitation lasers, comparable to “pulsed interleaved excitation” [54] or “alternating-laser excitation” [55] techniques. This will allow to filter spectral crosstalk and enable us to perform ratiometric Förster resonance energy transfer imaging [56]. Also an additional splitting of the fluorescence signal by polarization can be implemented to measure spatially resolved fluorescence anisotropy and its correlations [57]. Faster image sensors, such as scientific complementary metal-oxide semiconductor (sCMOS) cameras [30] and large-scale single-photon avalanche diode (SPAD) arrays (such as described in [34,58]), will allow much higher temporal resolution, matching that of confocal FCS. Today these sensors are still lacking in photosensitivity. Finally an extension to 3D-mapping of mobility and interaction parameters is easily possible by subsequently measuring several slices of a sample, although this will introduce a slice to slice time-structure.

Acknowledgments

The project was supported by a NUS-BW (National University of Singapore / Baden-Württemberg) joint grant to T.W. and J.L., a doctoral fellowship of the Heidelberg Graduate School of Mathematical and Computational Methods for the Sciences to J.W.K., a doctoral scholarship by the National University of Singapore to A.P.S. The authors thank Gabriele Müller and Antonija Burčul for preparing many of the cells and Nathalie Schwarz for preparing and labeling the 607 bp dsDNA, measured for this paper. We thank Yong Hwee Foo for 40 bp dsDNA oligos, Jagadish Shankarn for GUVs and Radek Machan for valuable comments and help on the dual labeled SUVs. The authors thank György Vámosi, Péter Brázda, Katalin Toth, Christian Fritsch and Nikoletta Szalóki for helpful discussions and testing of the data evaluation software. We also gratefully acknowledge Dag von Gegerfelt for borrowing one of the lasers. We thank the reviewers for valuable suggestions on this manuscript. Jan Wolfgang Krieger and Anand Pratap Singh contributed equally to this work.